LETTER

Small particles dominate Saturn's Phoebe ring to surprisingly large distances

Douglas P. Hamilton[1], Michael F. Skrutskie[2], Anne J. Verbiscer[2] & Frank J. Masci[3]

Saturn's faint outermost ring, discovered in 2009 (ref. 1), is probably formed by particles ejected from the distant moon Phoebe[2,3]. The ring was detected[1] between distances of 128 and 207 Saturn radii (R_S = 60,330 kilometres) from the planet, with a full vertical extent of $40R_S$, making it well over ten times larger than Saturn's hitherto largest known ring, the E ring. The total radial extent of the Phoebe ring could not, however, be determined at that time, nor could particle sizes be significantly constrained. Here we report infrared imaging of the entire ring, which extends from $100R_S$ out to a surprisingly distant $270R_S$. We model the orbital dynamics of ring particles launched from Phoebe, and construct theoretical power-law profiles of the particle size distribution. We find that very steep profiles fit the data best, and that elevated grain temperatures, arising because of the radiative inefficiency of the smallest grains, probably contribute to the steepness. By converting our constraint on particle sizes into a form that is independent of the uncertain size distribution, we determine that particles with radii greater than ten centimetres, whose orbits do not decay appreciably inward over 4.5 billion years, contribute at most about ten per cent to the cross-sectional area of the ring's dusty component.

In the course of mapping the entire sky, NASA's WISE spacecraft[4] observed Saturn's outer Phoebe ring at a wavelength of 22 μm in June 2010 (Fig. 1). The ring appears in its entirety, spanning an area of sky nearly 7,000 times larger than Saturn itself. Discovered by the Spitzer Space Telescope[1] at wavelengths of 24 μm and 70 μm, the Phoebe ring was recently detected at optical wavelengths by Cassini[5]. To highlight the faintest outer material, we suppress the vertical dimension and construct radial traces of the ring in Fig. 2 (Methods). Our measurements show that the ring extends to at least $270R_S$, well beyond the moon Phoebe, which traverses the region $180–250R_S$. The ring is also clearly seen inward to at least $100R_S$ (Fig. 1a) and to perhaps $50R_S$ (Fig. 1b) before being lost in the glare from Saturn.

To model the ring's structure, we follow the orbital motions of dust grains of multiple sizes launched from Phoebe at different points along its orbit. The most important forces affecting dust in the Phoebe ring are solar radiation pressure and the much weaker Poynting–Robertson drag[1–3]. Both of these forces arise from interactions with sunlight: the first due to the absorption of solar photons and the second primarily to the slightly asymmetric re-emission of the absorbed energy[6]. Radiation pressure causes dust grain eccentricities to oscillate with a period of approximately 30 years and is important for grains with radii $s < 100$ μm. These grains form a distribution that is offset towards the Sun, but still left–right symmetric. Poynting–Robertson drag, although extremely weak, imparts an important systematic inward decay towards Saturn with a characteristic timescale of $1.5 \times 10^5(s)$ years, where s is in units of μm; hence a 3-cm particle will evolve from Phoebe (with semimajor axis $a = 215R_S$) inward to the moon Iapetus ($a = 60R_S$) over the age of the Solar System[1].

We use the numerical code dI (dust Integrator[7–11]) to predict the orbits of particles with radii ranging from 4 μm to 10 m released from Phoebe. We launch dust grains with radii of 4, 6, 10, 15, 25, 40, 60 and

100 μm and with eight different angular positions of Phoebe's pericentre relative to the Sun, an important parameter when radiation pressure is strong. For larger grains, we continue to use five logarithmically spaced sizes per decade in radius, but follow only a single launch condition, as the dynamics of large grains are only weakly affected by radiation pressure. To speed up the integrations, we artificially enhance the rate of Poynting–Robertson drag by a factor ranging from 10 to 450. This results in rapid but otherwise identical orbital evolution as long as the inward drag timescale remains much longer than all other important timescales. We verified that this approximation is valid for our integrations.

We stop the integrations when the dust grains cross the orbit of Titan at $20R_S$ because collisions with that massive satellite occur within ~10,000 years, far shorter than the timescale for inward migration by Poynting–Robertson drag, even for the smallest particles. Grains with $s > 150$ μm remain on fairly low-eccentricity orbits, and so we stop those integrations when they reach Iapetus' orbit—this is an excellent approximation since the inward drag timescale exceeds the Iapetus collision timescale of a few million years. But since the WISE images
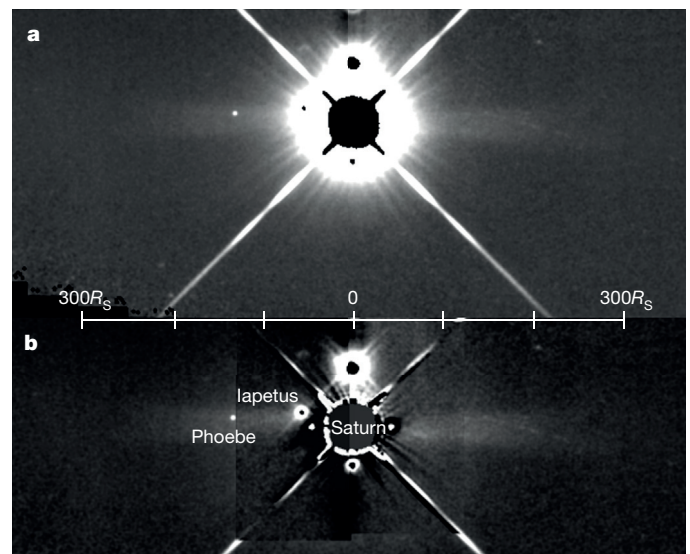

Figure 1 | WISE Band 4 mosaic of the Phoebe ring. a, Individual WISE frames manually combined: scattered light from Saturn forms the large white overexposed blob with a black centre while four diagonal diffraction spikes radiate outward. Bright reflections of Saturn are visible as smaller white lumps with black centres at the six and twelve o'clock positions. Iapetus (black dot) and the more distant Phoebe (white dot) are visible at nine o'clock. The Phoebe ring is the white, horizontally oriented $550R_S \times 40R_S$ rectangle. **b**, We subtract ±90° rotations of the top frame from itself, yielding clean and cluttered ring ansae (the apparent ends of edge-on rings); here we stitch the two clean ansae together to significantly reduce scattered light and reveal the ring's inner regions. Distance scale applies to **a** and **b**.

[1]Department of Astronomy, University of Maryland, College Park, Maryland 20742-2421, USA. [2]Department of Astronomy, University of Virginia, Charlottesville, Virginia 22904-4325, USA. [3]Infrared Processing and Analysis Center, Caltech, Pasadena, California 91125, USA.
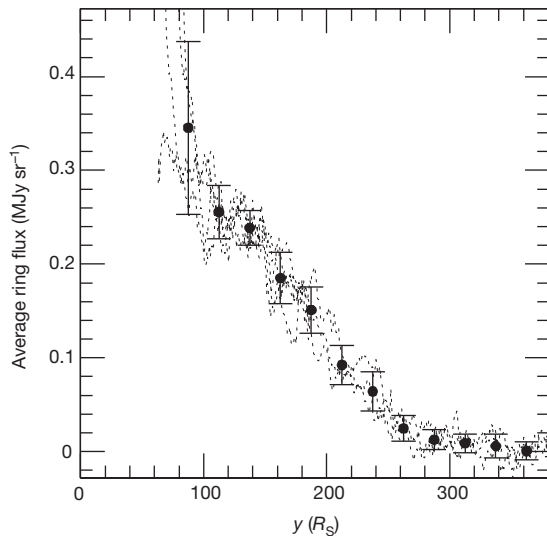
Figure 2 | Measured radial profiles. We sum over 30 × 40 pixel regions in Fig. 1 and subtract a sky signal as described in Methods to obtain one-dimensional radial profiles from each side of Fig. 1a and b. A fifth curve is derived directly from the WISE Image Atlas. All curves agree to within their intrinsic scatter which provides an important consistency check. Accordingly, the solid black data points with error bars represent the average and the scatter from our five measurements. Ring flux is clearly detectable to at least $270R_S$, well beyond Phoebe's apocentre distance of $250R_S$. All ring profiles agree well inward to about $100R_S$, at which point scattered light from Saturn becomes problematic.

Figure 3 | Theoretical radial profiles for 4–100 μm size distributions. We plot differential power-law particle size distributions with indices $q = 1$, 2 and 3 (dotted lines), 4 and 5 (solid line), and $q = 6$ (dashed line). A $q = 3$ power-law index puts an equal mass of ring particles in each logarithmic size interval; $q = 2$ does the same for surface area. We compute radial profiles for individual particle sizes from our numerical modelling and then combine them with different assumed power-law production rates, normalizing all curves to pass near the data point at $140R_S$. The shallow power-law size distributions (dotted lines) dominated by large particles are a poor match to the data, while steep size distributions more closely match.

only provide trustworthy fluxes outside about $100R_S$ (Figs 1 and 2), the comparison of data to theory is rather insensitive to the exact details of how the collisional sweeping of Iapetus at $60R_S$ is modelled.

Next, for each simulation we match the WISE viewing geometry by transforming the numerical data (a list of positions versus time for the lifetime of the integration) into a Saturn-centred reference frame that rotates so that the Sun always stays along the x axis. We view this distribution of dust from the direction of the Sun to produce an artificial y–z image on the sky that closely matches the geometry of Fig. 1. We sort the evenly-spaced output from our numerical simulations into line-of-sight bins, sum over the vertical dimension z, and produce predicted profiles of flux versus the y coordinate for each individual grain size whose dynamics we model. For the smallest dust grains, we average the distributions from the eight different Phoebe launch azimuths to get realistic profiles. Finally, we sum together distributions for individual grain sizes with different weighting functions. For simplicity, we assume that particles are continuously created at Phoebe according to a power-law size distribution of the form $N(s)ds \propto s^{-q}ds$, where $N(s)$ is the number of particles of radius s in the range $[s, s + ds]$ and q is the power-law index. This procedure correctly weights the contribution of all particle sizes to the ring flux by explicitly convolving the production function with orbital dynamics including particle lifetimes. The results are theoretical predictions that we normalize to the observed profiles of Fig. 2.

In Fig. 3, we limit particle sizes to the range from 4 μm, the smallest grains whose orbits are not all immediately forced by radiation pressure onto Titan-crossing orbits, to 100 μm, roughly the largest size where radiation pressure still matters. All distributions have some difficulty matching the two data points with $y < 120R_S$. These points are the most strongly affected by scattered light from Saturn and by our imperfect subtraction of this scattered light (Fig. 1). Focusing our attention on the more distant points, we note that the steepest power-law distributions ($q = 4$–6) fit the data best, highlighting the relative importance of small particles. Such steep particle size distributions are unusual in the Solar System. Nevertheless, steep size distributions of particles launched from Phoebe provide a satisfactory fit to the data.
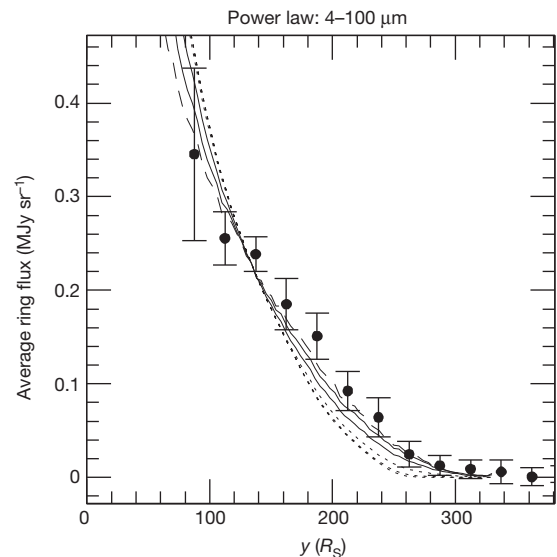
As steep power-law distributions are somewhat surprising, we test the effect of the upper cutoff size by raising it above 3 cm, to include ring particles that do not decay inward to Iapetus over the age of the Solar System. For example, 30-cm debris from Phoebe should be confined between $160R_S$ and $250R_S$, perhaps in sufficient quantities to improve the fit of the shallower power-law distributions in that region. In Fig. 4, we extend the size distribution up to 30 cm and find that the shallow power-law distributions, which highlight the contribution of 3–30 cm grains, are dramatically affected. Centimetre-sized material produces a ring with a largely empty interior region which, when viewed edge-on, leads to diminished flux close to the planet.

The shallow power-law distributions, however, predict rings that end abruptly at $250R_S$, Phoebe's apocentre, in contrast to the data. Instead of immediately ruling these distributions out, we instead consider relaxing another of our model assumptions. A promising improvement would be to include Phoebe family members (small satellites with Phoebe-like orbital inclinations[12,13]) as additional sources of ring material. Interestingly, these satellites are all more distant than Phoebe itself. While the known satellites comprise <1% of Phoebe's cross-sectional area, undiscovered 100-m sized and even kilometre-sized objects could raise this percentage significantly, making this population a correspondingly more important source of ring material. The most relevant effect of these additional sources on the theoretical ring profiles of Fig. 4 would be to raise the predicted ring flux outside $250R_S$ to more closely match the observations.

Two further assumptions might be relaxed. First, the size distribution of particles produced in the ring need not follow a power law, and second, the distribution of particle sizes may be modified by mutual collisions as the material drifts inward towards Iapetus. Collisions are most important for large particles that would otherwise remain in orbit for hundreds of millions to billions of years. Accordingly, shallow power laws with indices of $q = 1$–2, or indeed any other distribution dominated by large particles, would probably evolve towards a more typical collisional distribution with index $q = 3$–4. For these reasons, we continue to favour the steeper size distributions.

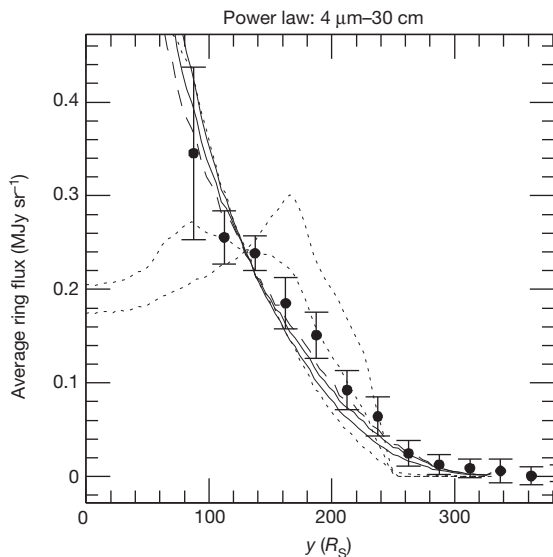**Figure 4 | Theoretical radial profiles for 4 µm–30 cm size distributions.** The curves are predictions for assumed differential power-law particle size distributions, as in Fig. 3. Shallow size distributions (dotted lines) predict a ring dominated by large particles, with diminished flux from the ring's interior due to the reduced grain mobility. A distribution with power index $q = 1$, with large particles producing 90% of the observed ring flux, predicts a peak at $170R_S$ that is clearly inconsistent with the data. By contrast, index $q = 2$, with 20% of the flux from 3–30 cm particles, perhaps adequately matches the data, at least interior to Phoebe's apocentre at $250R_S$. Distributions with steeper power-law indices still match the data best.

True particle sizes in the ring, however, are skewed by the enhanced infrared emission of the smallest particles. Because the peak wavelength of a blackbody thermal emission spectrum (~35 µm for ~80 K) is significantly larger than the smallest grains in the ring, these particles emit long-wavelength radiation inefficiently. Thus, the temperatures of small particles rise, more energy is emitted at shorter wavelengths, the emission peak rises and moves closer to the WISE 22 µm band, and the measured flux increases significantly. This drives our best fits towards steeper power-law indices, as the fits actually represent convolutions of the true particle size distribution residing in the ring with the enhanced emission expected from small and relatively hot dust grains.

All of these considerations are suggestive of more complicated size distributions. A broken power law[14] with temperature effects included for the smallest particles would be a logical next step. However, its application is complicated by the fact that the position of the break and the change in the power-law index both depend sensitively on assumptions about the radiating efficiency of the probably irregularly-shaped ring particles. Furthermore, collisions amongst ring particles and with interplanetary debris, sputtering by the solar wind, sand-blasting by

tiny interstellar dust grains, and other unmodelled loss mechanisms are also likely to affect the ring's current particle size distribution. Accordingly, it makes sense to convert the constraints of Fig. 4 into a form independent of any assumed size distribution: we find that soccer-ball-sized and larger rocks ($2s > 20$ cm) do not evolve significantly inward over the age of the Solar System and, accordingly, cannot account for more than ~10% of the observed ring flux.

Online Content Methods, along with any additional Extended Data display items and Source Data, are available in the online version of the paper; references unique to these sections appear only in the online paper.

1. Verbiscer, A. J., Skrutskie, M. F. & Hamilton, D. P. Saturn's largest ring. *Nature* **461,** 1098–1100 (2009).
2. Burns, J. A., Hamilton, D. P., Mignard, F. & Soter, S. in *Physics, Chemistry and Dynamics of Interplanetary Dust* (eds Gustafson, B. A. & Hanner, M. S.) 179–182 (ASP Conference Series, Kluwer, 1996).
3. Tamayo, D., Burns, J. A., Hamilton, D. P. & Hedman, M. M. Finding the trigger to Iapetus' odd global albedo pattern: dynamics of dust from Saturn's irregular satellites. *Icarus* **215,** 260–278 (2011).
4. Wright, E. L. *et al.* The Wide-field Infrared Survey Explorer (WISE): mission description and initial on-orbit performance. *Astrophys. J.* **140,** 1868–1881 (2010).
5. Tamayo, D., Hedman, M. M. & Burns, J. A. First observations of the Phoebe ring in optical light. *Icarus* **233,** 1–8 (2014).
6. Burns, J. A., Lamy, P. L. & Soter, S. Radiation forces on small particles in the solar system. *Icarus* **40,** 1–48 (1979).
7. Hamilton, D. P. Motion of dust in a planetary magnetosphere: orbit-averaged equations for oblateness, electromagnetic, and radiation forces with application to Saturn's E ring. *Icarus* **101,** 244–264 (1993).
8. Hamilton, D. P. Erratum: Motion of dust in a planetary magnetosphere: orbit-averaged equations for oblateness, electromagnetic, and radiation forces with application to Saturn's E-ring. *Icarus* **103,** 161 (1993).
9. Hamilton, D. P. & Kruger, H. The sculpting of Jupiter's gossamer rings by its shadow. *Nature* **453,** 72–75 (2008).
10. Jontof-Hutter, D. & Hamilton, D. P. The fate of sub-micron circumplanetary dust grains I: Aligned dipolar magnetic fields. *Icarus* **218,** 420–432 (2012).
11. Jontof-Hutter, D. & Hamilton, D. P. The fate of sub-micron circumplanetary dust grains II: Multipolar fields. *Icarus* **220,** 487–502 (2012).
12. Gladman, B. *et al.* Discovery of 12 satellites of Saturn exhibiting orbital clustering. *Nature* **412,** 163–166 (2001).
13. Hamilton, D. P. Planetary science: Saturn saturated with satellites. *Nature* **412,** 132–133 (2001).
14. Brooks, S. M., Esposito, L. W., Showalter, M. R. & Throop, H. B. The size distribution of Jupiter's main ring from Galileo imaging and spectroscopy. *Icarus* **170,** 35–57 (2004).

Author Contributions F.J.M. led the development of the WISE Image Atlas products and provided optimally background-matched custom mosaics to support this analysis. M.F.S. and A.J.V. did the image processing and data analysis associated with Figs 1 and 2. D.P.H. performed the analytic calculations, ran the numerical models, and produced the theoretical curves of Figs 3 and 4.

Author Information Reprints and permissions information is available at www.nature.com/reprints. The authors declare no competing financial interests. Readers are welcome to comment on the online version of the paper. Correspondence and requests for materials should be addressed to D.P.H. (dphamil@umd.edu).

METHODS

In the course of its all-sky mid-infrared survey, the NASA Wide-field Infrared Survey Explorer (WISE[4]) scanned over the position of Saturn 12 times between UT 2010-06-12.85 and UT 2010-06-13.98. Extended Data Fig. 1 shows a subset of the WISE Band 4 (22 μm) 'Level 1B' individual frames that captured ring flux and did not have significant artefacts from Saturn's scattered light. Note that the wavelength of Band 4 has been revised upward from 22.1 μm to 22.8 μm (ref. 15). WISE scanned the sky systematically driven in ecliptic longitude by the steady precession of its orbit of about 1° per day, so from orbit to orbit the position of Saturn shifts several arcminutes across the 47-arcmin-wide frame. Saturn's orbital motion of 1.6 arcmin during the observing period is minor compared with this rate of spacecraft precession. Saturn itself spans only a couple of WISE pixels, so scattered light dominates the 'image' of Saturn on the scale of several arcminutes. In the upper two rows of Extended Data Fig. 1, the bright object embedded in the ring east (left) of Saturn is Phoebe. The ring flux is faint in the individual exposures (~3 DN per pixel at 160 Saturnian radii (R_S) compared with pixel-to-pixel RMS noise from the background of 10 DN; DN indicates Digital Number). The ring emission spans ~50 pixels in vertical extent and is hundreds of pixels wide, so averaging over the spatial dimension as well as stacking individuals frames substantially improves the accuracy of the flux estimate. The pixel scale of the WISE Band 4 Level 1B images is 5.5 arcsec per pixel.

Atlas Images. WISE data products include an Image Atlas that optimally combines Level 1B individual frames into a final calibrated image registered to the celestial reference frame. Given the large spatial extent of the Phoebe ring (~300R_S radius or ~40 arcmin), image smearing of the Phoebe ring in the Atlas Images due to Saturn's 1.6 arcmin motion relative to the stellar background is minor compared with extent of the ring flux and small compared with the bins used for fitting of the ring flux in the main text. Two WISE All-Sky Atlas Image fields contain ring flux. In one (1800p030, Extended Data Fig. 2), Saturn lies off the edge of the image and the ring flux is largely uninfluenced by the proximity of Saturn. The adjacent Atlas Image (1784p030) contains Saturn itself, and the excessive flux from the planet caused significant corruption of the faint ring flux and underlying background flux, rendering this automatically generated Image Atlas frame largely useless for determining ring properties.

Custom co-additions. Given the availability of the individual Level 1B exposures contributing to the atlas images, a selection of Level 1B exposures not significantly corrupted by the flux from Saturn itself were offset to compensate for Saturn's motion on the sky and combined with a σ-rejected average to produce another representation of the WISE ring image (Extended Data Fig. 3). In this case, ring flux was reconstructed with fidelity both east and west of Saturn.

Ring flux estimation. Extended Data Fig. 3 shows the region of the ring, as well as background regions above and below the ring, isolated in strips 50 pixels in extent in the latitude direction (perpendicular to the ring). The flux in the ring region was estimated in a series of 8-pixel-wide bins in the longitude direction by calculating the median of the pixel values in each 8 × 50 pixel region while subtracting the average of the background medians from similar regions above and below the ring. Overall, three ring profiles resulted from extraction from the 1800p030 Atlas Images (ring east side) and the east and west sides of the full image in Extended Data Fig. 3. These profiles are largely independent, as the most significant noise source is the systematic level background offsets resulting from imperfect matching of the offset level in the individual Level 1B frames. These profiles show no evidence of east–west ring asymmetry.

Subtraction of scattered light from Saturn at small radii. The ring profile extractions outlined above suffer from contamination from excess scattered light from Saturn at small separations from the planet. Under the assumption that the scattered light is symmetric about the origin, additional profiles were constructed by rotating the image assembled from the individual Level 1B frames by 90° and subtracting it from itself (bottom half of Fig. 1). Doing so reveals structure (including a clear view of Iapetus) hidden previously by scattered light. The fidelity of this subtraction is only as good as the assumption that the scattered flux is symmetric, since the residual ring profile close to Saturn is a small fraction of the scattered flux being subtracted. Extended Data Fig. 4 shows the result of applying this technique to the bright point source Alpha Tau from the Band 4 WISE Image Atlas. The subtraction is free of significant artefacts that would bias ring flux extraction, and reveals subtle background matching offsets at the 0.2 DN level. Figure 2 contains an east-side and a west-side ring flux extraction from the rotated self-subtracted imagery that partially overlaps the extractions from the wider-field mosaics described above.

Non-uniform backgrounds. Structure in the background arising from zodiacal dust emission and galactic backgrounds could bias the ring flux measurements described above. Extended Data Figs 5–7 illustrate that the Band 4 background is smooth on the scales addressed above, and that the smooth gradient in background in the ecliptic latitude direction is small compared with the ring flux on the scales that impact the extracted flux. Given that there is a gradient in zodiacal emission increasing from north to south, it is possible that the 90° rotation will shift zodiacal background inappropriately from one ecliptic latitude to another. Fortunately, over the spatial scale of interest the zodiacal emission is nearly constant (becoming largely uniform in the lower portion of the image corresponding to high line number in Extended Data Fig. 6).

Assumptions underlying the model fit. As the ring is optically thin, each point in the radial profile measured in Fig. 2 contains contributions from ring material orbiting at a range of distances from Saturn. We could, in principle, continue to process the data by mathematically removing successive outer layers of ring material to determine the material's intrinsic radial distribution[16,17]. This approach, however, has two serious disadvantages. First, errors in removing outer layers build up to strongly affect results for the inner layers, especially if the data are relatively noisy as in these WISE images. But even more importantly, the orbits of particles in the Phoebe ring are strongly influenced by radiation pressure and hence expected to be highly elliptical. Thus the distribution of debris in the Phoebe ring deviates from the cylindrical symmetry required by standard data reduction techniques. Accordingly, we choose to proceed by building up entirely theoretical radial profiles of the Phoebe ring to compare directly to the data.

Sample size. No statistical methods were used to predetermine sample size.

Code availability. We have opted not to make available the numerical codes used to produce Figs 3 and 4, both because the codes were not designed to be easily portable and because we anticipate numerous significant upgrades in the next year.

15. Brown, M. J. I., Jarrett, T. H. & Cluver, M. E. Recalibrating the Wide-field Infrared Survey Explorer (WISE) W4 filter. *Publ. Astron. Soc. Austral.* 31, e049 (2014).
16. Showalter, M. R., de Pater, I., Verbanac, G., Hamilton, D. P. & Burns, J. A. Properties and dynamics of Jupiter's gossamer rings from Galileo, Voyager, Hubble and Keck images. *Icarus* 195, 361–377 (2008).
17. Hedman, M. M., Burns, J. A., Hamilton, D. P. & Showalter, M. R. The three-dimensional structure of Saturn's E ring. *Icarus* 217, 322–338 (2012).
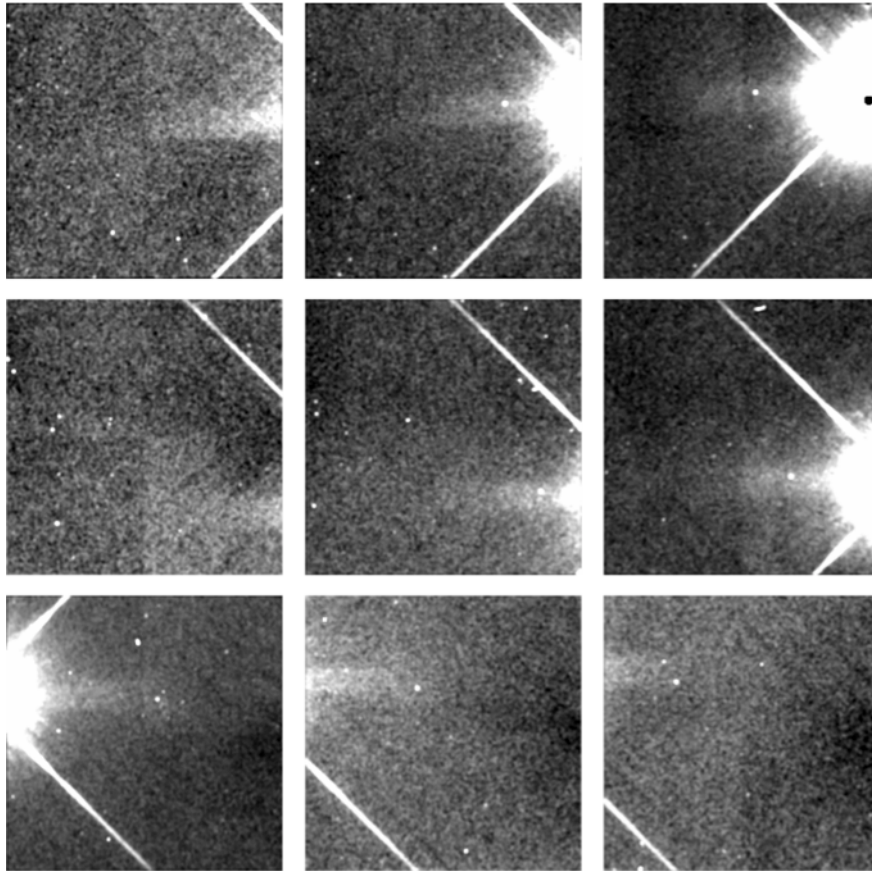
Extended Data Figure 1 | Ring flux in a subset of single (Level 1B) WISE Band 4 (22 μm) exposures. We organize these nine independent images so that each row contains three images centred at approximately the same ecliptic latitude (vertical direction). For each row, spacecraft orbital precession shifts Saturn in the ecliptic longitude direction so that the planet moves from left to right. The vertical ring extent is about 50 pixels and the horizontal extent exceeds 200 pixels, so even the single exposures can be binned to yield modest signal to noise ratio on the ring.
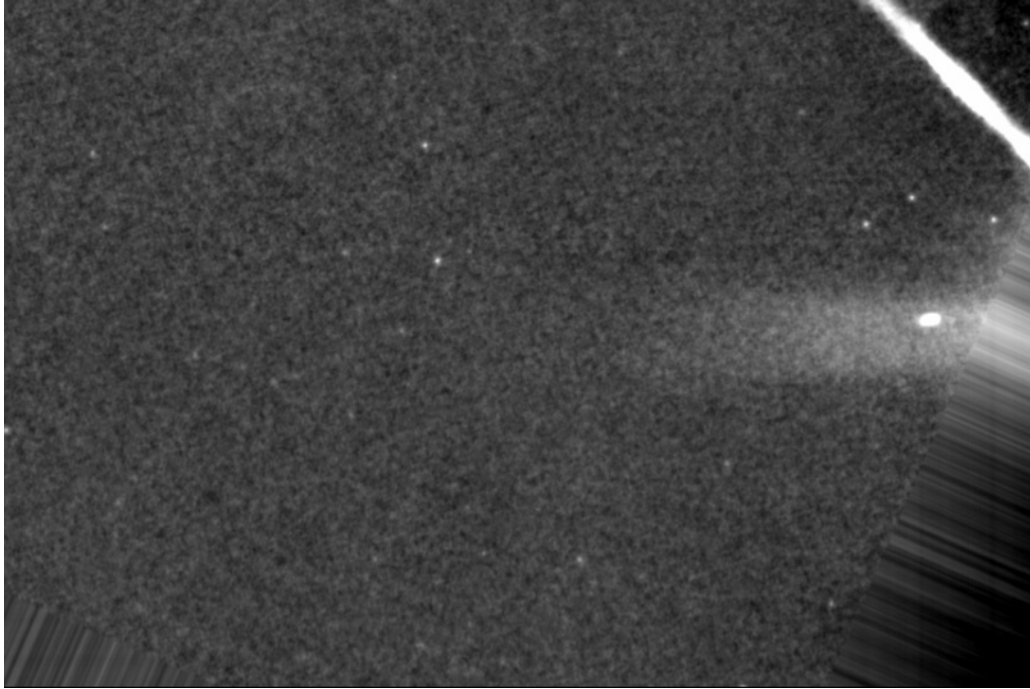
Extended Data Figure 2 | A portion of the WISE Image Atlas frame containing ring emission. The image is rotated so that ecliptic north is up and east is to the left. In this Atlas Image, the bright emission from Saturn is outside the WISE field of view, but one of its diffraction spikes is visible at top right; processing artefacts to the bottom left and right should be ignored. The ring flux (horizontal stripe) is uncontaminated by Saturn's scattered light, although the orbital motion of Saturn smears the embedded image of Phoebe into a bright oval. The faint point sources are distant stars and galaxies.
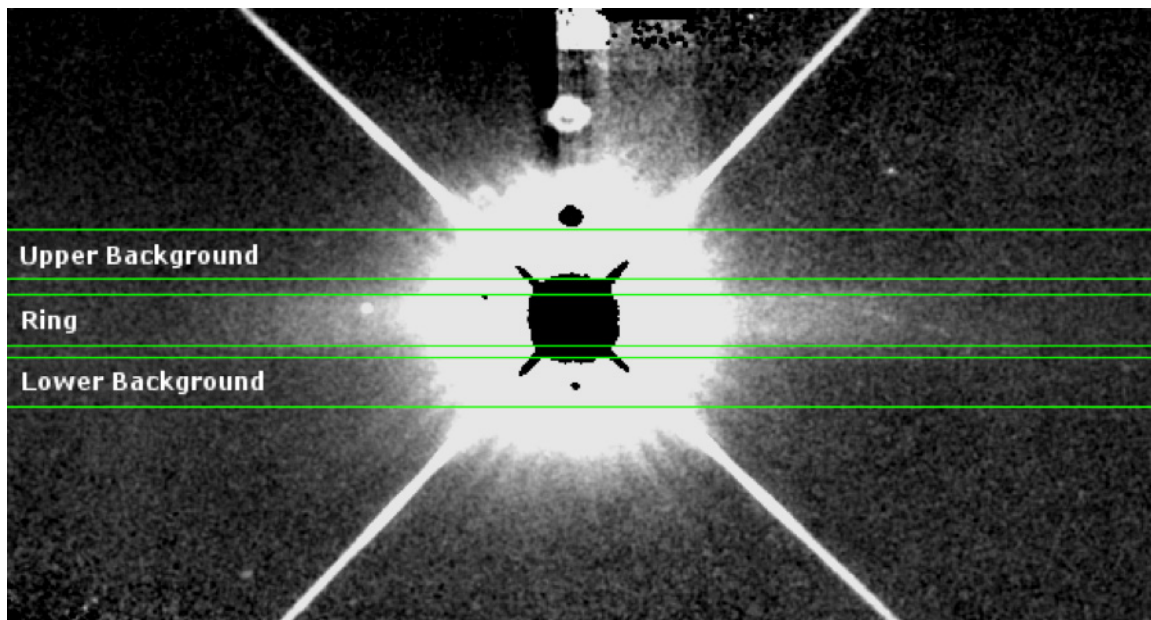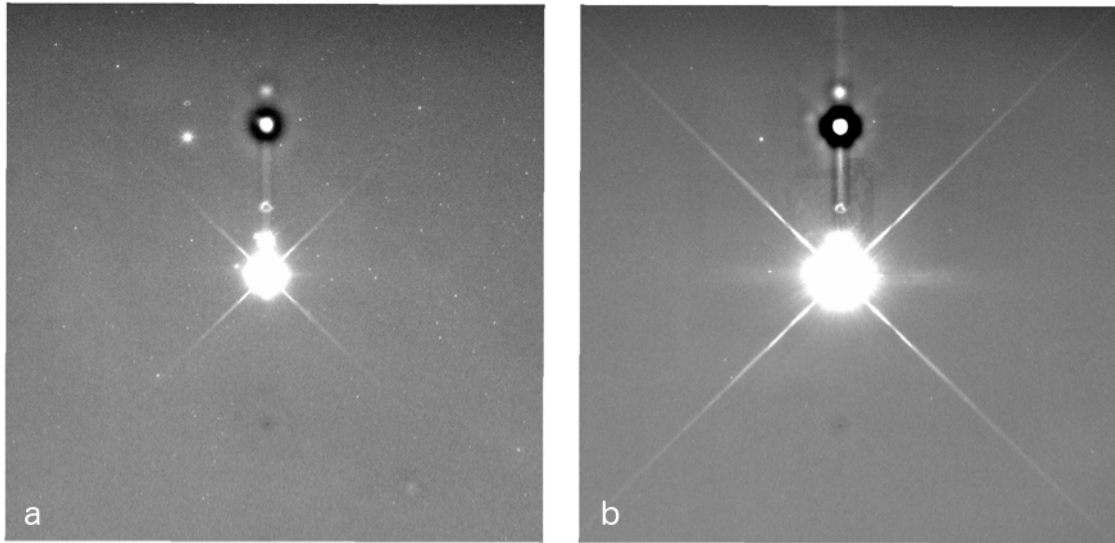
Extended Data Figure 3 | A custom WISE Band 4 mosaic produced from selected Level 1B frames. Each selected Level 1B image was free from significant artefacts from Saturn's scattered light. The frames have been shifted, offset to a common background level and stacked with trimmed average pixel filtering in Saturn's frame of reference (so that Phoebe, the point source on the east/left side of the ring, appears unsmeared). Ecliptic north is up and east is to the left. Green lines highlight the regions used for flux extraction.
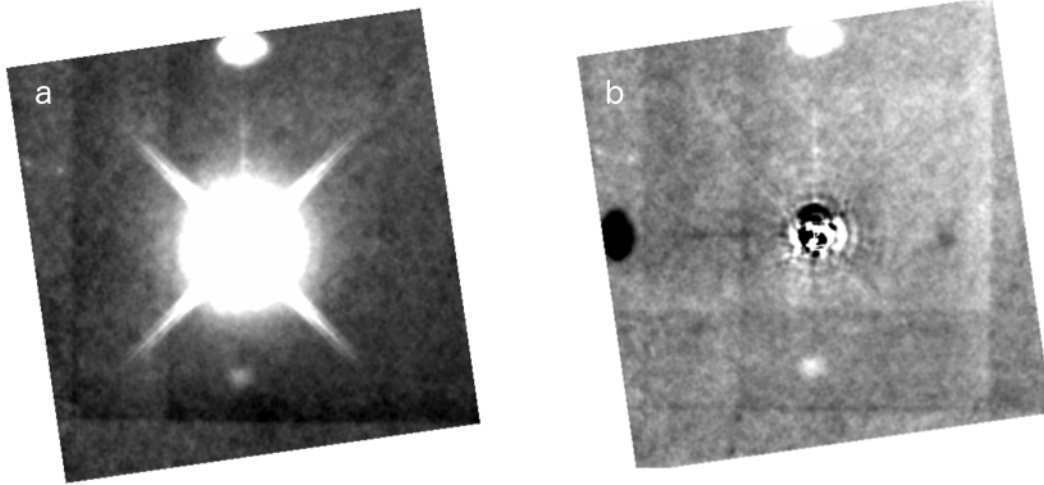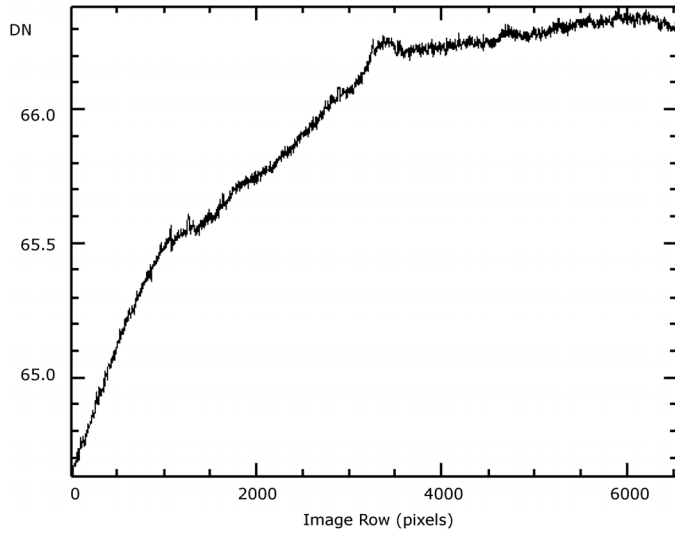
Extended Data Figure 4 | WISE Band 4 images of the star Alpha Tau.
a, Direct image of the star. **b**, The same image rotated by 90° and subtracted from itself mitigating scattered light. The large blob-shaped artefacts up, down, left and right from the central star are due to the reflection of starlight from the telescope's internal structure. Significant artefacts from azimuthally asymmetric scattered flux near the star, by contrast, are not evident in the subtracted image **b**. Residuals after subtraction arise largely from frame offset mismatch and are typically of order 0.2 DN in the image in **b** (compared with 3 DN for the ring flux at $160R_S$).

Extended Data Figure 5 | Examination of background structure. a, A WISE Band 3 (12 μm) optimally frame-matched mosaic oriented in ecliptic coordinates with north up and east to the left. **b**, Band 4 (22 μm) optimally frame-matched mosaic. The ring is evident in the middle of the Band 4 image, extending left and right horizontally from the central white over-exposed image of Saturn. The backgrounds are largely uniform, especially in Band 4, with the exception of a north–south gradient characteristic of zodiacal dust emission. Ring flux is not obviously evident in the 12 μm Band 3 exposure.

Extended Data Figure 6 | Quantitative analysis of Band 4 background gradient in units of DN. This figure plots the average background level in DN (vertical axis) row-by-row (horizontal axis) in the Band 4 image shown in Extended Data Fig. 5. The analysis region slightly overlaps the ring flux, which appears as the small bump around line 3300 and establishes the ring plane. The sense of the rotation used in the 90° subtraction carries flux from line numbers 3500–4000 into the ring midplane. Because the DN values are so similar, the bias introduced by the rotation is no greater than 0.1 DN while the inner ring flux is of order 6 DN.
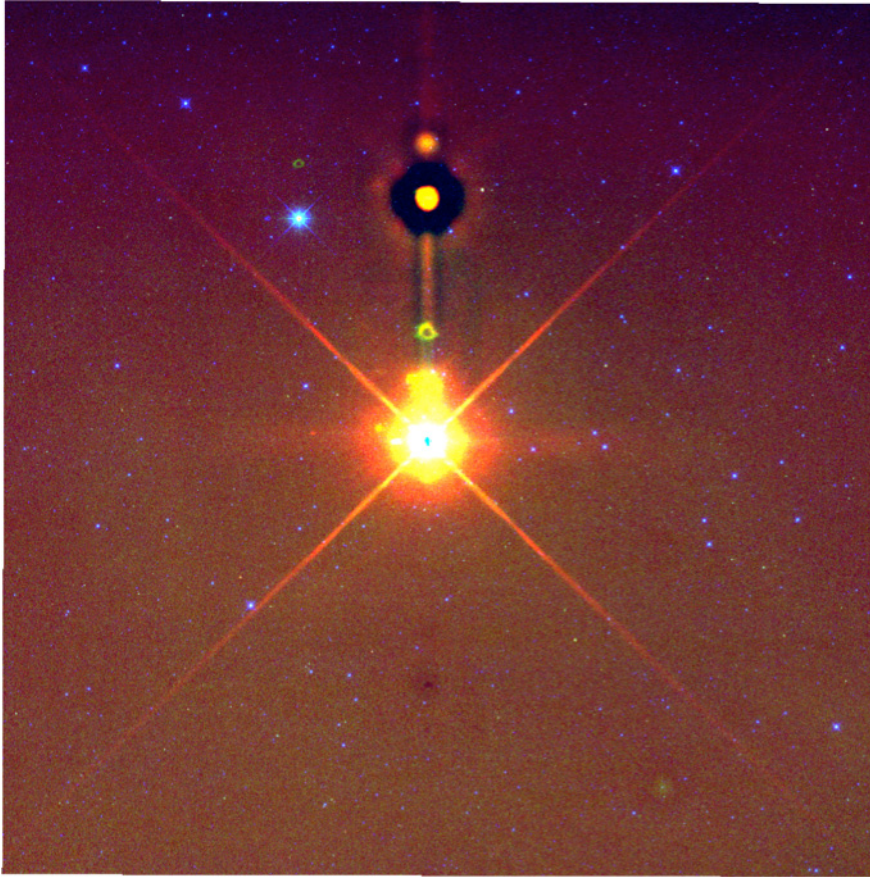
Extended Data Figure 7 | Colour composite of the Phoebe ring. Mosaics of images in WISE Bands 2, 3 and 4 (4.6, 12 and 22 μm) comprise the composite image in ecliptic coordinates. North is up and east is to the left. Scattered light from Saturn forms the bright white circle at the centre of the image and the ring is the faint horizontal bar that cuts across Saturn.